CRYSTAL GROWTH & DESIGN

pubs.acs.org/crystal

Article

Open Access

This article is licensed under CC-BY 4.0

Isostructural Tin and Germanium Carbonates ($Sn[CO_3]_2$ and $Ge[CO_3]_2$)

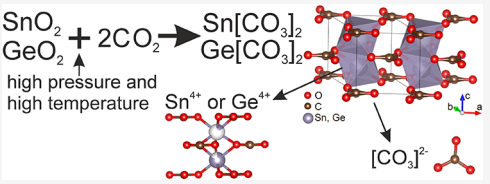
Lkhamsuren Bayarjargal,* Dominik Spahr, Elena Bykova, Valentin Kovalev, Victor Milman, Nico Giordano, and Björn Winkler

Cite This: *Cryst. Growth Des.* 2026, 26, 5436−5445

Read Online

ACCESS | Metrics & More | Article Recommendations | Supporting Information

ABSTRACT: Tin and germanium carbonates, $Sn[CO_3]_2$ and $Ge[CO_3]_2$, were synthesized by the reaction of SnO_2 or GeO_2 with CO_2 at high pressures and high temperatures in a laser-heated diamond anvil cell. Their structures were solved by in situ single-crystal X-ray diffraction at high pressures. $Sn[CO_3]_2$ formed at ∼30 GPa, while $Ge[CO_3]_2$ formed at around 44 GPa. Both carbonates are isostructural and crystallize in the trigonal space group *P*3. The distinguishing feature of the $Sn[CO_3]_2$ or $Ge[CO_3]_2$ structures is the presence of isolated $[CO_3]^{2-}$ groups, which are arranged in layers. Both structures contain octahedrally coordinated tetravalent Sn^{4+} and Ge^{4+} cations in two positions with partial site occupation. Bulk moduli of both carbonates are $K_0 \approx 44-48$ GPa. Full geometry optimizations based on DFT calculations reproduced the crystal structures. The DFT models were used to complement the experimental compression data and for the assignment of Raman modes. Both Sn and Ge carbonates can be recovered under ambient conditions after pressure release.



INTRODUCTION

Isostructural carbonates are crystals that share the same structure but differ in their chemical composition, showing the flexibility of carbonate topologies. They provide valuable insights into how cation size and charge affect structural stabilities, which is particularly important for understanding mineral formation and the high-pressure behavior of carbonates.[1,2] The high-pressure behavior of carbonates has been extensively studied because they are the primary carbon reservoirs in the Earth's crust and play a central role in the long-term global carbon cycle.[3] They facilitate the transport of carbon from the Earth's crust into the deep Earth and help balance the carbon budget between the planet's surface and interior.[3]

At ambient conditions, more than 120 anhydrous carbonate minerals, termed "conventional" carbonates, and characterized by trigonal $[CO_3]^{2-}$ groups, are known.[3−5] Of these, more than 21 are chemically simple carbonates containing a single cation. Carbonates of Ca, Mg, and Fe dominate this group, comprising over >90% of carbonate minerals in the Earth's crust.[3] These divalent-cation carbonates are isostructural with either the calcite ($R\bar{3}c$) or aragonite ($Pmcn$) structure type, where $[CO_3]^{2-}$ groups are arranged in layers.[6,7] These two structure types are particularly important because they allow systematic cation substitutions over a wide compositional range.[7] For these carbonates with divalent cations (M^{2+}), the ionic radius of the cation plays a key role in determining whether the carbonate crystallizes in the calcite or aragonite structure type. At ambient pressure, carbonates containing cations with ionic radii ≤ 1.00 Å in 6-fold coordination (*C.N.* = 6), such as Mg^{2+} and the 3*d* transition-metal cations (e.g., Ni^{2+} and Fe^{2+}), as well as Ca^{2+} and Cd^{2+} cations, adopt the calcite structure type.[7,8] The stability field of the calcite structure at ambient pressure corresponds to cation radii ranging from 1.00 to 0.69 Å. The lower limit of this range is defined by Ni, which has the smallest cation radius ($r_{Ni^{2+}}$ = 0.69 Å). At higher pressures, however, even smaller cations such as Be^{2+} ($r_{Be^{2+}}$ = 0.45 Å) can adopt the calcite structure.[9] The higher limit of this range is defined by Ca^{2+}, which has an ionic radius of 1.00 Å (in *C.N.* = 6) and represents a borderline case. $CaCO_3$ is found in both structure types. In contrast, carbonates hosting larger cations, such as Sr^{2+} and Ba^{2+}, with ionic radii in the range of 1.15−1.35 Å, typically crystallize in the aragonite structure type with cations in 9-fold coordination (*C.N.* = 9).[6−8]

Anhydrous carbonates containing a single type of monovalent or divalent metal cation are common in nature. Cations with valence states higher than +2 are typically incorporated through coupled substitutions with monovalent or divalent cations in complex natural carbonate minerals.[4] Chemically simple carbonates incorporating cations with valences greater than +2 have only been synthesized under high-pressure conditions. Examples include carbonates containing trivalent cations, such as $Al_2[CO_3]_3$, $Fe_2[CO_3]_3$, and $Cr_2[CO_3]_3$, which host Al^{3+}, Fe^{3+}, and Cr^{3+} cations, respectively.[10−12] Even more

Received: March 13, 2026
Revised: June 16, 2026
Accepted: June 24, 2026
Published: July 1, 2026



ACS Publications

© 2026 The Authors. Published by American Chemical Society

Downloaded from pubs.acs.org/cgdefu/article-pdf/26/14/5436/6531695/2/acs.cgd.6c00352.pdf by DEUTSCHES ELEKTRONEN-SYNCHROTRON user on 09 November 2026

recently, we reported the synthesis of an iodide carbonate, $(IO_2)_2[CO_3]$, in which iodine adopts a + 5 oxidation state.[13]

Within the class of tetravalent cations, $Ti[CO_4]$ and $Ti_2O_3[CO_3]$ represent the first simple carbonates containing tetravalent cations.[14] More recently, we synthesized uranium carbonates $U_2[CO_3]_3$ and $U[CO_3]_2$ with a trivalent and tetravalent uranium cation, respectively, at high pressures.[15] Among the tetravalent cations, the group 14 elements silicon (Si^{4+}), germanium (Ge^{4+}), and tin (Sn^{4+}) are particularly noteworthy. Silicon is the second most abundant cation (22%) in the Earth's mantle after Mg (23%).[16] The recent discovery of $Si[CO_3]_2$ demonstrates that more carbonates with tetravalent cations can be obtained and reveals that a silicon carbonate may be present in the deep Earth.[17] The abundance of Sn and Ge in the Earth is significantly smaller than that of silicon. Therefore, Sn- or Ge-bearing carbonates have limited relevance to geoscience. However, they are highly interesting from a crystal-chemical perspective. The cation radius of silicon is 0.40 Å, whereas Sn and Ge exhibit larger cation radii of 0.69 and 0.53 Å, respectively. However, due to the large variation in the ionic radii, it is not obvious if Si, Ge, and Sn carbonates would be isostructural. Nevertheless, these compounds can exhibit strong structural analogies for pressure-induced phase transitions. In the case of oxides, such analogies have been identified among SnO_2, GeO_2, and SiO_2. For SiO_2 in the stishovite (rutile-type) structure, the reported sequence of pressure-induced phase transitions follows the order: rutile-, $CaCl_2$-, α-PbO_2-, and $Pa\bar{3}$-type polymorphs.[18−20] SnO_2 and GeO_2 exhibit an analogous transition phase sequence.[21−24] If such structural analogies can also be identified in carbonates, they could provide a useful basis for extrapolating crystal-chemical correlations at high pressures and for benchmarking theoretical predictions. Up to now, tin or germanium carbonates have neither been predicted nor synthesized. The successful synthesis and characterization of anhydrous Sn and Ge carbonates would therefore represent a significant extension of the known crystal chemistry of carbonates.

The aim of the present study is to explore the formation of chemically simple anhydrous carbonates with tetravalent Sn^{4+} and Ge^{4+} cations. We present the successful synthesis, characterization by Raman spectroscopy, and X-ray diffraction of two new carbonates with the composition $Sn[CO_3]_2$ and $Ge[CO_3]_2$ and discuss their properties.

METHODS

High-Pressure Experiments

We used synthetic SnO_2 (99.9% purity, Alfa Aesar) and GeO_2 (99.998% purity, Aldrich Chemical Co.) for the high-pressure experiments. The high-pressure experiments were carried out in diamond anvil cells (DACs) with a Boehler-Almax design and a 300 μm culet size.[25] We used rhenium as a gasket material, which was preindented to a thickness of ~45 μm. 120 μm gasket holes serving as sample chambers were drilled by a custom-built laser setup.

Compacted powders with maximum dimensions of up to ~100 × 40 × 15 μm^3 and a ruby for pressure determination were placed in the gasket hole. Then, CO_2 was directly condensed into the sample chamber using a custom-built cryogenic loading system. In order to condense the CO_2 into the sample chamber, a slightly opened DAC was placed on a liquid nitrogen-cooled Cu holder, which enabled us to cool down the DAC to ~100 K. We used a small nozzle to direct a CO_2 gas jet directly on the diamonds and the gasket.[13] Ar was used as a purge gas to avoid the precipitation of H_2O ice. The precipitation of the CO_2 in the gasket hole was monitored using an optical microscope. After a sufficient amount of CO_2 was gathered in the sample chamber, the DAC was tightly closed. CO_2 dry ice is less compressible than Ne or He, and hence the gasket hole does not shrink notably during compression.

The pressure was determined by measuring the shift of the ruby fluorescence, assuming a potential error of 6% due to deviations from hydrostatic conditions.[26] We estimate a pressure uncertainty of at least ~10% due to the pressure gradient and pressure change after laser heating.

Raman Spectroscopy and Laser Heating

The sample was laser-heated from both sides using a custom-built setup equipped with a CO_2 laser (Coherent Diamond K-250, λ = 10,600 nm).[27] The laser power was adjusted to achieve a coupling of the laser to the sample, using a laser power of 1−6 W, resulting in a maximum temperature of 2600(300) K. The focus on the sample results in a heating area of ~40 × 40 μm^2. The temperatures during the laser heating were determined by the two-color pyrometer method, employing Planck and Wien fits. Heating procedures in DACs may suffer from large temperature gradients, and the actual temperature is strongly dependent on the coupling of the laser with the sample. We estimate an uncertainty of at least ~ 10% of the nominal temperature in the laser-heated region, depending on specific laser heating conditions, based on typical 2D temperature-gradient determination experiments performed in DACs.[28]

Raman spectroscopy at high pressures was performed using a custom-built setup and a commercial Raman spectrometer (Oxford Instruments WITec α 300R). The custom-built setup was equipped with a Nd:YAG laser (λ = 532.14 nm, Cobolt-Samba, Hübner Photonics) and a spectrometer (Princeton Instruments ACTON SpectraPro, SP-2356, with a Pixis 256E CCD camera).[27] We used a Raman laser spot size on the sample of ~6 μm while using a laser power of 250 mW on the sample. The commercial Raman system was equipped with a UHTS 300S (VIS-NIR) spectrograph in combination with an Andor DR316B-LDC-DD CCD detector. The measurements were performed with a 532 nm laser and a power of <100 mW. Two-dimensional Raman maps were measured with an Olympus SLMPan N 50x objective on a regular grid with a grid spacing of 3 μm. The background correction was performed using the software package Matlab. The Raman mode positions and their corresponding full widths at half-maximum (fwhm's) were extracted from the experimental Raman spectra by fitting the spectra with a Lorentzian function using the Fityk software.[29]

Synchrotron Single-Crystal Diffraction

Single crystal X-ray diffraction was performed at the PETRA III synchrotron (DESY) in Hamburg, Germany, on the extreme conditions beamline P02.2.[30] The beam size on the sample was ≈2 × 2 μm^2 (fwhm), focused by Kirkpatrick Baez mirrors. The diffraction data were collected using a PerkinElmer XRD1621 detector using a wavelength of 0.290 Å. We collected single-crystal data while rotating the DAC by ± 33° around the axis perpendicular to the beam, while collecting frames in 0.5° steps with 4 s acquisition time per frame.

The detector-to-sample distances (405 and 400 mm) were calibrated with a CeO_2 standard using DIOPTAS.[31] At each experimental session, the instrument calibration was done using data collected from a single crystal of enstatite ($MgSiO_3$). After the measurement, the reflections were indexed and integrated employing CrysAlis^{PRO}. We used the Domain Auto Finder program (DAFi) to find possible single-crystal domains for the subsequent data reduction.[32] The crystal structures in this study were solved using SHELXT.[33,34] After structure solution, the crystal structures were refined with SHELXL.[35] SHELXT and SHELXL programs were implemented in the Olex2 software package.[36]

Density Functional Theory-Based Calculations

First-principles calculations were carried out within the framework of density functional theory (DFT), employing the Perdew−Burke−Ernzerhof (PBEsol) exchange-correlation functional and the plane wave/pseudopotential approach implemented in the CASTEP simulation package.[37−39] CASTEP and associated programs for

Downloaded from pubs.acs.org/cgdefu/article-pdf/26/14/5436/6531695 2/acs.cgd.6c00352.pdf by DEUTSCHES ELEKTRONEN-SYNCHROTRON user on 09 November 2026

https://doi.org/10.1021/acs.cgd.6c00352
Cryst. Growth Des. 2026, 26, 5436−5445

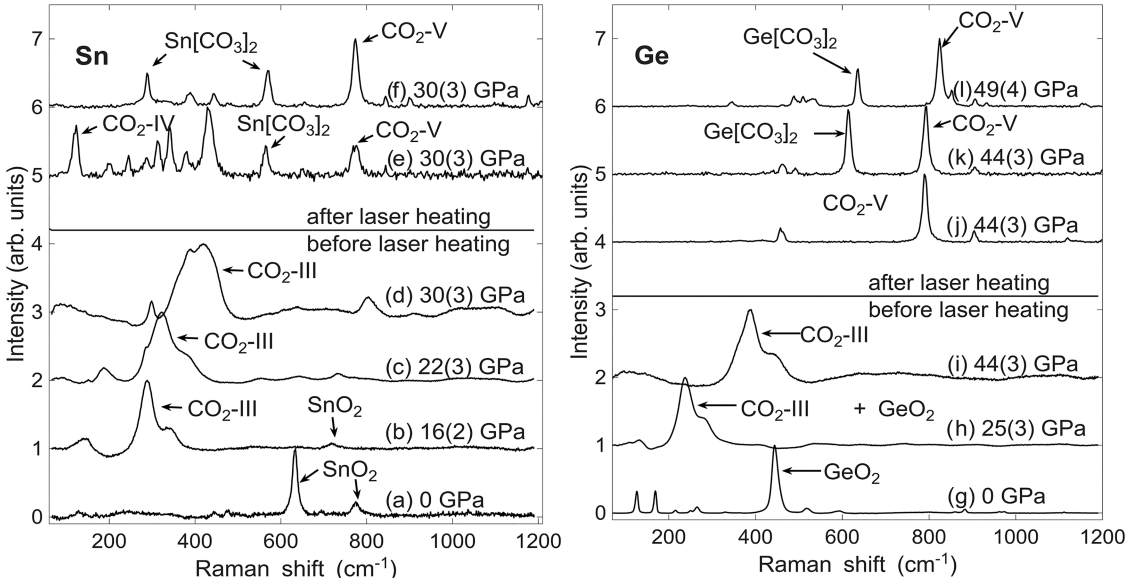


Figure 1. Characteristic peaks for each phase are indicated by arrows. Raman spectra of starting SnO_2 (a) and GeO_2 (g) at ambient conditions. Raman spectra of SnO_2 + CO_2 (b–d) and GeO_2 + CO_2 (h, i) during compression without heating. At 30(3) GPa, the sample was measured after laser heating at different positions, labeled (e) and (f). At position (e), in addition to the Raman spectra of $Sn[CO_3]_2$, contributions from both CO_2–IV and CO_2–V were observed. In the center of the heated area, position (f), the Raman spectra were dominated by CO_2–V and $Sn[CO_3]_2$. After laser heating, the sample was measured at different positions (j, k, l) at 44(3) GPa and 49(3) GPa. Some positions (j) contain only the CO_2–V phase. The appearance of Raman bands near 613 cm^{-1} at 44(3) GPa and 636 cm^{-1} at 49(3) GPa indicates the formation of $Ge[CO_3]_2$ in addition to CO_2–V in positions (k) and (l).

symmetry analysis and visualization were run within the BIOVIA Materials Studio suite of programs.[40] "On the fly" norm-conserving (for phonon calculations) or ultrasoft (for p-V calculations) pseudopotentials generated using the descriptors in the CASTEP database were employed in conjunction with plane waves up to a kinetic energy cutoff of 1020 or 630 eV, for norm-conserving and ultrasoft pseudopotentials, respectively. The accuracy of the pseudopotentials is well established.[41] A Monkhorst–Pack grid was used for Brillouin zone integrations.[42] We used a distance between grid points of <0.023 $Å^{-1}$. Convergence criteria for geometry optimization included an energy change of $<5 \times 10^{-6}$ eV $atom^{-1}$ between steps, a maximal force of <0.008 eV $Å^{-1}$ and a maximal component of the stress tensor <0.02 GPa.

Elastic stiffness coefficients were obtained by the strain–stress method. In the stress–strain method employed here, symmetry-adapted strain patterns were imposed on the fully optimized ground state structure. For each symmetry-adapted strain, atomic coordinates were relaxed, and the stress tensor was obtained for three to six different amplitudes. Elastic coefficients and their statistical errors were obtained from linear fitting of the stress–strain dependencies.[43] Phonon frequencies were obtained from density functional perturbation theory (DFPT) calculations.[44,45] Raman intensities were computed using DFPT with the "2n+1" theorem approach.[46] Typical experimental fwhm values of Raman modes range from 4 to 10 cm^{-1}. Accordingly, we set the theoretical fwhm to 5 cm^{-1} based on our practical experience.

RESULTS AND DISCUSSION

Compression and Heating of SnO_2 + CO_2 and GeO_2 + CO_2

Compression and heating experiments of mixtures SnO_2 + CO_2 and GeO_2 + CO_2 were performed in three distinct runs. For SnO_2 + CO_2, the sample was initially compressed to 22 GPa without intermediate heating. During compression, Raman spectroscopy indicated a phase transition of CO_2 from CO_2–I ($Pa\bar{3}$) to CO_2–III ($Cmca$) (Figure 1b–d).[47−49] CO_2–III was present prior to laser heating and partially transformed into CO_2–IV upon laser irradiation.[50] No carbonate formation was observed after heating at 22 GPa. The sample was subsequently compressed to 30 GPa and laser-heated again. After laser heating, new Raman modes appear in the region 280–580 cm^{-1} in addition to the Raman modes of CO_2–V ($I\bar{4}2d$)[51] and indicate a reaction leading to a new Sn carbonate phase (Figure 1f). Residual CO_2–IV phase was still observed in some regions (Figure 1e).

At ambient conditions, SnO_2 crystallizes in the rutile-type structure, which was identified by characteristic Raman modes at 633 and 774 cm^{-1} (Figure 1a).[52] With increasing pressure, SnO_2 undergoes a series of structural phase transitions to denser crystal forms.[21,23] The first transition occurs around 12 GPa, where the rutile structure transforms into an orthorhombic $CaCl_2$-type structure and afterward α-PbO_2-type structure. With further increase in pressure, typically above 21 GPa, it transforms into the $Pa\bar{3}$-type polymorph. Unfortunately, the Raman signals of SnO_2 were very weak after the loading with CO_2 (Figure 1b), preventing clear identification and reliable tracking of the pressure-induced phase transitions using Raman spectroscopy (Figure 1c,d). In contrast, X-ray diffraction enabled the identification of high-pressure polymorphs of SnO_2 in the $Pa\bar{3}$-structure type at 33(3) GP after heating, which was still observed during decompression a pressures of 22(2) GPa and 15(2) GPa, and consistent with previous studies.[21,23]

In the case of GeO_2 + CO_2, the characteristic Raman modes of GeO_2 were detected at 125, 169, and 444 cm^{-1} at ambient conditions (Figure 1g), which demonstrates that the starting GeO_2 adopts the quartz-type crystal structure.[53] After loading the GeO_2 sample with CO_2, the Raman signals from GeO_2 became very weak and were difficult to detect (Figure 1h,i). We were able to track phase transitions in CO_2 only, while those in GeO_2 could not be detected by Raman spectroscopy. We do not know why the Raman intensity drops dramatically after the CO_2 is introduced into the sample chamber.

Downloaded from pubs.acs.org/cgdefu/article-pdf/26/14/5436/6531695 2/acs.cgd.6c00352.pdf by DEUTSCHES ELEKTRONEN-SYNCHROTRON user on 09 November 2026

https://doi.org/10.1021/acs.cgd.6c00352
Cryst. Growth Des. 2026, 26, 5436–5445

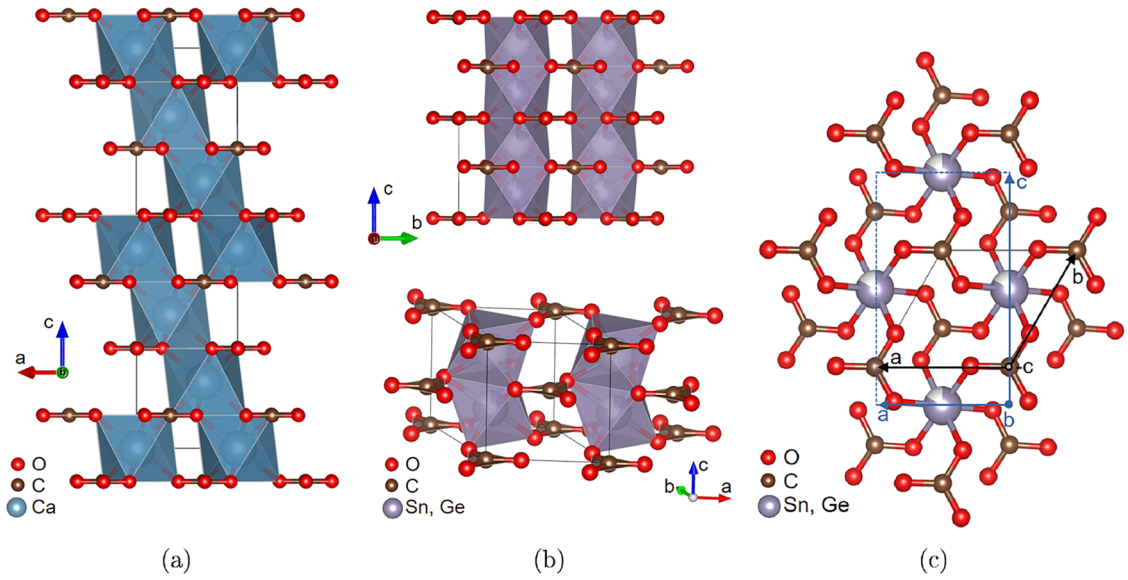


Figure 2. (a) Structure of calcite, $Ca[CO_3]$, at 0 GPa. (b) Structure of $Sn[CO_3]_2$ at 32(3) GPa or $Ge[CO_3]_2$ at 51(4) GPa, viewed along [100] and [010]. Sn and Ge carbonates are isostructural. The structure contains isolated CO_3 groups and SnO_8 octahedra or GeO_8 octahedra. (c) Projection of the crystal structure of $Sn[CO_3]_2$ and $Ge[CO_3]_2$ with the symmetry of *P*3 along the *c* axis at 32(3) GPa and at 51(4) GPa, respectively. The unit cell and axis of both carbonates are represented with black lines. The figure illustrates the relation of both structures with monoclinic $Si[CO_3]_2$-$P2_1/n$. The unit cell of $Si[CO_3]_2$ is outlined by the blue dashed line. The images of crystal structures were created using VESTA software.[55]

According to a previous study, GeO_2 transforms to a $P2_1/c$ monoclinic phase with increasing pressure and remains stable up to 52 GPa.[54] Heating this phase at around 33−36 GPa induced a transformation into the $CaCl_2$-type structure.[24,54] Above 41 GPa, the $CaCl_2$-type structure of GeO_2 further transforms into the α-PbO_2-type structure.[24,54] Our X-ray diffraction experiments allowed the identification of high-pressure polymorphs of GeO_2 in the $CaCl_2$ structure type at around 30(3) GPa and the α-PbO_2 structure type at 50(4) GPa. This is consistent with the previous results.[22,24,54] While laser heating of the $GeO_2 + CO_2$ mixture at 32(3) GP does not lead to a formation of carbonates, heating to 2600(300) K at higher pressures of 44(4) GPa and 51(4) GPa induces the formation of a new Ge carbonate.

After laser heating (Figure 1) of both samples, spatially resolved Raman spectroscopy was employed to identify chemical reaction products and to determine the spatial distribution of previously unknown phases. A more detailed description of the Raman measurements is provided later in the section on Raman spectroscopy. The location of the new phases by Raman spectroscopy allowed us to efficiently search for them by X-ray diffraction, which was carried out to determine the crystal structures of the unknown phases.

Structure of $Sn[CO_3]_2$

Analysis of the synchrotron single-crystal X-ray diffraction data revealed that the unknown phase is a carbonate with the composition $Sn[CO_3]_2$. Using the synchrotron single crystal data, the crystal structure of the phase was determined. A total of 224 independent reflections with intensities $I > 2\sigma(I)$ were measured, and 25 parameters were refined. The resulting reflection-to-parameter ratio (9:1) ensured a reliable and robust structure refinement. The *wR* value after the refinement was 7.0%. $Sn[CO_3]_2$ crystallizes in the trigonal space group *P*3 (No. 143) with $Z = 1$ (Figure 2b). The lattice parameters at 32(3) GPa are $a = b = 4.3880(13)$ Å, $c = 4.391(3)$ Å, $\gamma = 120°$ and $V = 73.22(7)$ Å^3. The crystallographic parameters and details of the structure refinement of $Sn[CO_3]_2$ measured at 32(3) GPa are listed in Tables S1−S3.

This crystal structure contains isolated $[CO_3]^{2-}$ groups and Sn^{4+} cations. The Sn atoms are octahedrally coordinated by oxygen and occupy two Wyckoff locations (1/3, 2/3, 0.241 and 1/3, 2/3, 0.73) with an approximate occupation of 0.853(4) and 0.147(4), respectively. These partial occupancies gave a total tin content of 1 per formula unit, and this maintains the charge balance. According to a previous study on Si carbonate, an inversion of these site occupancies produces an equivalent structure with a shifted origin. For the major site with occupancy of 0.853(4), Sn−O distances range from 1.93(5) Å to 2.03(5) Å. The average Sn−O distance is 1.97(3) Å. The site with minor occupancy of 0.147(4) has slightly shorter Sn−O distances of 1.92(7) Å and 1.97(7) Å. These interatomic distances are well within the range of typical Sn−O bond lengths in SnO_2-$Pa\bar{3}$, which were measured by us at 30 GPa.[21] The coordination SnO_6 polyhedra and $[CO_3]^{2-}$ groups are illustrated in Figure 2b. Each SnO_6 polyhedra is connected to the others through shared faces, forming a linear, chain-like network. In contrast, the CaO_6 polyhedra in calcite are connected to each other by a shared edge and are arranged in a staggered pattern (Figure 2a).

In $Sn[CO_3]_2$, the $[CO_3]^{2-}$ groups are arranged in layers parallel to the *c*-axis and located on (002) planes. The C−O bond lengths within the carbonate groups are approximately ∼1.27(5) Å or ∼1.25(5) Å, with the O−C−O angles of $\phi_1^{O-C-O} = 120.0(2)°$. The average C−O bond length (∼1.245 Å) is consistent with that reported for the bond length of $Si[CO_3]_2$. The crystallographic data of $Sn[CO_3]_2$ has been deposited in the Cambridge Structural Database (CSD) under the deposition number CCDC 2531455.

The structural parameters derived from experiments were employed as a trial structure in DFT calculations. The structure after the full geometry optimization was in good agreement with the experimental values, as the DFT calculations gave $a = b = 4.4418$ Å, $c = 4.3628$ Å, $\gamma = 120°$,

https://doi.org/10.1021/acs.cgd.6c00352
Cryst. Growth Des. 2026, 26, 5436−5445

Downloaded from pubs.acs.org/cgdefu/article-pdf/26/14/5436/6531695/2/acs.cgd.6c00352.pdf by DEUTSCHES ELEKTRONEN-SYNCHROTRON user on 09 November 2026

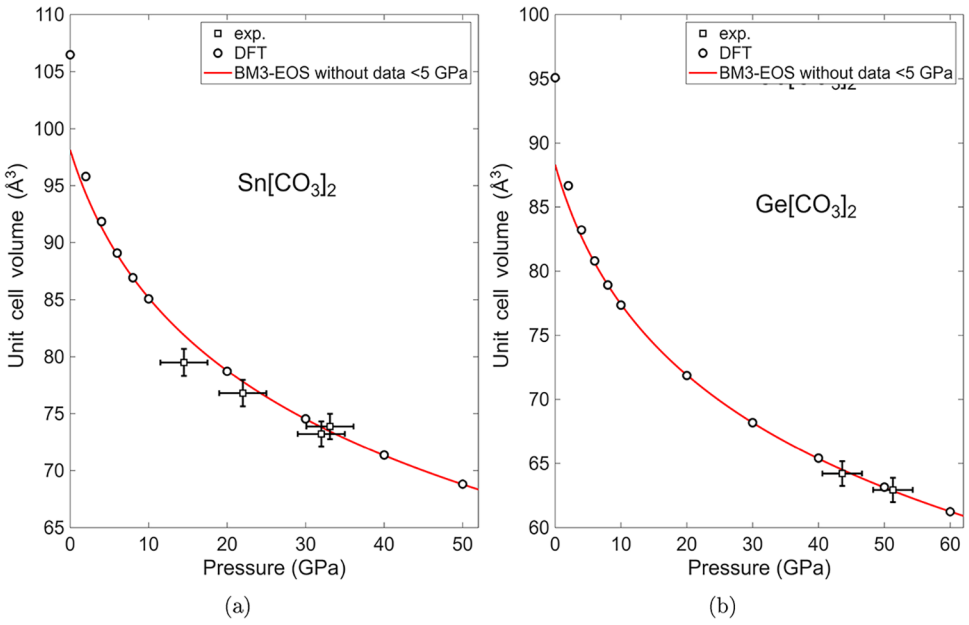


Figure 3. Pressure dependence of the unit-cell volumes of $Sn[CO_3]_2$ (a) and $Ge[CO_3]_2$ (b). Squares represent the experimental data of $Sn[CO_3]_2$ and $Ge[CO_3]_2$, while circles denote the DFT data. The red lines represent the BM3-EOS fit obtained by excluding DFT data below 5 GPa.

and V = 74.54 Å^3 (Tables S1 and S4) at 30 GPa. DFT calculations were performed based on a fully ordered structure with site occupancies of 1 and 0 for the tin atoms.

Structure of $Ge[CO_3]_2$

The crystal structure solution and refinement of the new phase from the GeO_2 + CO_2 experiment revealed that it is a germanium carbonate with the composition $Ge[CO_3]_2$. The structure refinement converged with a wR-value of 7.2%. At 51(4) GPa, $Ge[CO_3]_2$ crystallizes in the trigonal space group $P3$ with $a = b = 4.1952(9)$ Å, $c = 4.1262(6)$ Å, $\gamma = 120°$ and $V = 62.89(3)$ Å^3. The structure of $Ge[CO_3]_2$ is isostructural to $Sn[CO_3]_2$ and is shown in Figure 2. The Ge^{4+} atoms are octahedrally coordinated by oxygen atoms. The structure contains two distinct $[CO_3]^{2-}$ groups with longer C−O bonds (~1.30(3) Å) and shorter C−O bonds (~1.19(3) Å). These differences are more pronounced than in $Sn[CO_3]_2$. The Ge−O distances range from 1.75(7) to 1.87(7) Å, with an average of 1.801 Å. The Ge atoms occupy two Wyckoff positions with site occupancies of 0.962(5) and 0.038(5). A similar imbalance in site occupancy was also observed in one of the crystals of $Si[CO_3]_2$.[56] The crystallographic parameters and details of the structure refinement of $Ge[CO_3]_2$ measured at 51(4) GPa are listed in Tables S5−S7. The crystallographic data of $Ge[CO_3]_2$ have been deposited in the Cambridge Structural Database (CSD) under the deposition number CCDC 2531456.

The structural model derived from the experiments was employed as a trial structure for DFT full geometry optimizations. The two data sets are in good agreement. A comparison can be found in Tables S5 and S8. Similar to the previous Sn carbonate, a fully ordered structure with site occupancies of 1 and 0 for the Ge atoms served as the basis for the DFT calculations of $Ge[CO_3]_2$.

Comparison of $Sn[CO_3]_2$, $Ge[CO_3]_2$, and $Si[CO_3]_2$

Both structural models of $Sn[CO_3]_2$ or $Ge[CO_3]_2$ exhibit a pseudo symmetry of $P\bar{6}$ or $P\bar{3}$ with a center of inversion. However, structural refinements performed in the centrosymmetric space group lead to significantly higher R and wR values compared to the noncentrosymmetric model. For example, refinement in $P\bar{3}$ results in an increase of the wR value from 7.0 to 11.4% for the $Sn[CO_3]_2$-$P\bar{3}$ model and from 7.2 to 8.5% for the $Ge[CO_3]_2$-$P\bar{3}$ model. Moreover, this refinement yields an unrealistic C−O bond length of approximately 1.50 Å. The pseudo symmetry of $P\bar{6}$ can result from a fully ordered model of Sn or Ge in which the unit cell parameter is doubled along the c-axis.

Spahr et al.[56] discovered $Si[CO_3]_2$ with a novel structure, which has a monoclinic $P2_1/n$ space-group symmetry. Here we illustrate (Figure 2c) the relationship between the monoclinic $P2_1/n$ structure of $Si[CO_3]_2$ and the $P3$ trigonal structure of $Sn[CO_3]_2$ and $Ge[CO_3]_2$. In $Si[CO_3]_2$, the $[CO_3]^{2-}$ groups are arranged in layers and tilted by 4° with respect to the (002) planes. The consequence of this out-of-plane tilting of $[CO_3]^{2-}$ groups is the reduction from the trigonal symmetry into the monoclinic $P2_1/n$ symmetry. We calculated Raman spectra of both Ge and Sn carbonates in the monoclinic $P2_1/n$ space group. Raman spectra calculated for both phases show that the $P2_1/n$ structure exhibits many more additional Raman peaks and weaker bands, reflecting the reduced symmetry and structural distortions. However, these calculated weak Raman bands were not observed, confirming the higher symmetry (see Figure S4).

Bulk Modulus and Compressibility of $Sn[CO_3]_2$ and $Ge[CO_3]_2$

The bulk modulus of both phases was obtained by fitting a third-order Birch−Murnaghan equation (BM3-EOS)[57,58] of states to volumes obtained by DFT-based calculations (Figure 3) using the EoSFit7 program.[59] In addition, the complete elastic stiffness tensor was obtained for $Sn[CO_3]_2$ and $Ge[CO_3]_2$ from stress−strain calculations at different pressures (see Section SI.5). The bulk moduli computed from the elastic stiffness tensor are shown in Table S9. A calculation of the complete elastic stiffness tensor by the stress−strain method for $Sn[CO_3]_2$ and $Ge[CO_3]_2$ indicated an extreme elastic anisotropy and very small values for c_{33} and c_{44} at 0 GPa (see Section SI.5). This would typically indicate that these phases

Downloaded from pubs.acs.org/cgdefu/article-pdf/26/14/5436/6531695/2/acs.cgd.6c00352.pdf by DEUTSCHES ELEKTRONEN-SYNCHROTRON user on 09 November 2026

https://doi.org/10.1021/acs.cgd.6c00352
Cryst. Growth Des. 2026, 26, 5436−5445

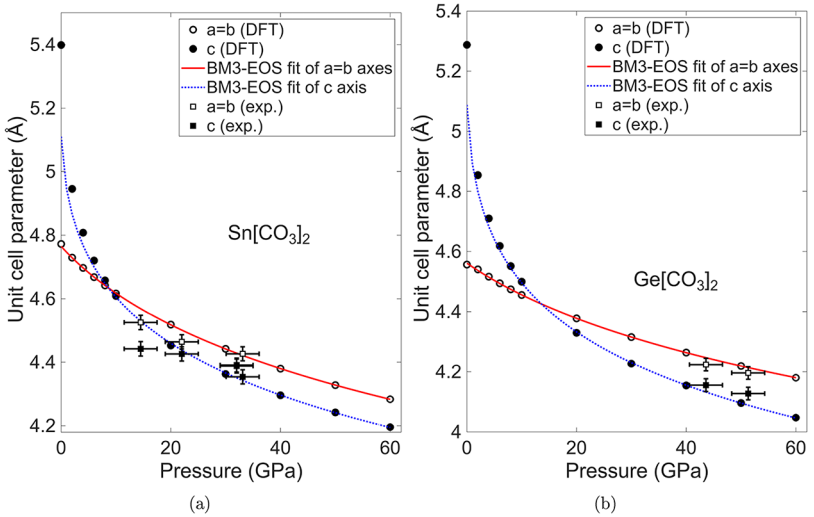


Figure 4. Pressure dependence of the unit-cell parameters of $Sn[CO_3]_2$ (a) and $Ge[CO_3]_2$ (b). Open symbols refer to the *a* and *b* unit-cell parameters, whereas black symbols represent the *c* unit-cell parameters. The dashed blue lines correspond to the BM3-EOS fit to the *c* unit-cell parameters, whereas the red lines represent the BM3-EOS fit to the *a* and *b* unit-cell parameters obtained by excluding data below 5 GPa.

are not stable at ambient conditions. This, however, is in contrast to the experimental observations and is very likely a consequence of the full cation order imposed in the DFT model. The c_{33} and c_{44} values calculated above $p \geq 2$ GPa are within the expected range. We therefore consider only values above 5 GPa to be representative, and only volumes for $p > 5$ GPa were employed for the EOS-fits. Excluding data for $p < 5$ GPa from the fits, the bulk modulus of $Sn[CO_3]_2$ is K_0 = 44(2)GPa (V_0 = 98.2(4) Å^3 and K_p = 6.9(2) while the bulk modulus of $Ge[CO_3]_2$ is K_0 = 48(3)GPa (V_0 = 88.3(4) Å^3 and K_p = 7.0(3))) (Figure 3).

Bulk moduli of both crystals indicate that they are more compressible than other carbonates adopting calcite- or aragonite-type structures.[60,61] For comparison, isostructural $Si[CO_3]_2$ exhibits a slightly higher modulus (53.1(4) GPa) than $Sn[CO_3]_2$ and $Ge[CO_3]_2$.[56]

The compressibility of $Sn[CO_3]_2$ and $Ge[CO_3]_2$ is very anisotropic. The pressure dependence of the unit-cell parameters is shown in Figure 4, whereas Figure S3 shows the relative change of the unit-cell parameters. Both figures demonstrate that the *c*-axes of both crystals are significantly more compressible than the *a* = *b*-axes in $Sn[CO_3]_2$ and $Ge[CO_3]_2$. This compressibility can be better quantified using linear moduli of the axes. The linear modulus of each axis was determined by fitting BM3-EOS to unit-cell parameters obtained by DFT-based calculations (Figure 4) using the EoSFit7 program for both phases.[59] Excluding data for $p < 5$ GPa from the fits, the linear modulus of *a* = *b*-axes of $Sn[CO_3]_2$ is M_0 = 251(3)GPa (a_0 = 4.7649(15) Å, and M_p = 15.1(2)) while the linear modulus of *c*-axes is M_0 = 14(2)GPa (c_0 = 5.110(fixed) Å, and M_p = 59(9)) (Figure 4a). The c_0 value was held fixed to obtain a reasonable fit. In the case of $Ge[CO_3]_2$ the linear moduli are M_0 = 360(3)GPa (a_0 = 4.5614(8) Å, and M_p = 14.7(2)) and M_0 = 13(1)GPa (c_0 = 5.088(fixed) Å, and M_p = 40(3)) for *a*- and *c*-axes, respectively (Figure 4b). The difference between the linear moduli of *a*- and *c*-axes is 1 order of magnitude for both crystals. This can be explained by the fact that, within the CO_3 layers, the rigid carbonate groups push against each other, thereby reducing the compressibility along the *a* = *b* directions during compression. Such pronounced anisotropy is typical in calcite-type structures where the weak bonding between the CO_3 layers dominates the compression behavior.[60]

Raman Spectroscopy

Spatially resolved Raman measurements allowed us to locate the individual phases in the DAC after laser heating. This is shown in Figure 5. The Raman map allowed us to select

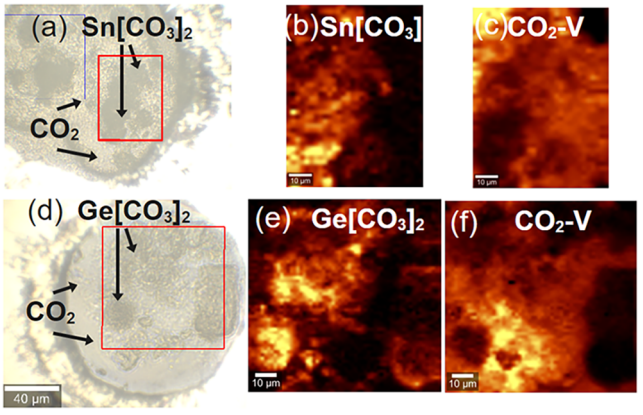


Figure 5. (a) Optical image of compacted SnO_2 powder and CO_2 in the DAC after laser heating at 30(3) GPa. The area in which spatially resolved Raman spectra were collected is indicated by a red square. (b) $Sn[CO_3]_2$ was located by mapping a Raman band at 571 cm^{-1}. (c) Raman map of CO_2–V (771 cm^{-1}). (d) Optical microscopic image of compacted GeO_2 powder and CO_2 in the DAC after laser heating at 49(4) GPa. After laser heating and temperature quenching, CO_2 and $Ge[CO_3]_2$ could be identified by Raman at this pressure. (e) Raman map of the 634 cm^{-1} band shows the location of $Ge[CO_3]_2$. (f) Distribution of CO_2–V was mapped by the band at 824 cm^{-1}.

regions in which mainly a single phase, either GeO_2 and SnO_2, CO_2–V, $Ge[CO_3]_2$, or $Sn[CO_3]_2$ could be measured. In Figure 6, experimental and DFPT-Raman spectra obtained at different locations in the DAC are compared to each other. As can be seen from Figure 6a, the most intense Raman band of $Sn[CO_3]_2$ can be found at ~571 cm^{-1} at a pressure of 30(3) GPa. Three further intense bands are located at ~289, 845, and 1178 cm^{-1}. During the pressure release at 0 GPa, the most

https://doi.org/10.1021/acs.cgd.6c00352
Cryst. Growth Des. 2026, 26, 5436−5445

Downloaded from pubs.acs.org/cgdefu/article-pdf/26/14/5436/6531695 2/acs.cgd.6c00352.pdf by DEUTSCHES ELEKTRONEN-SYNCHROTRON user on 09 November 2026

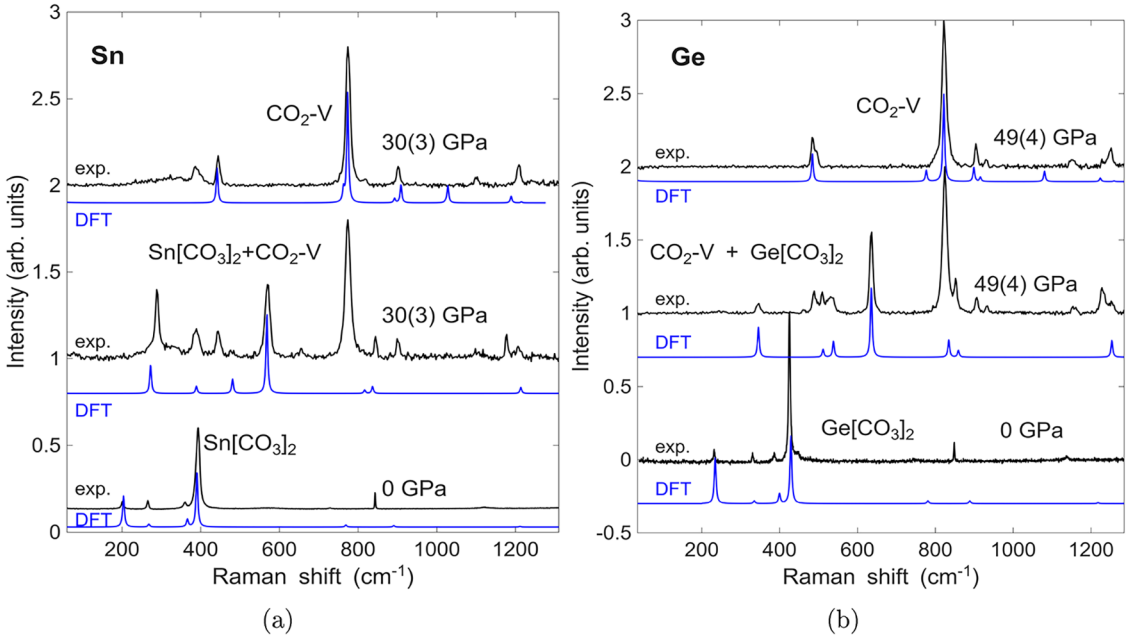


Figure 6. (a) Raman spectra of CO_2−V and $Sn[CO_3]_2$. Experimental Raman spectra (black line) were collected at 30(4) GPa after laser heating, quenched to ambient temperature. Theoretical (blue line) Raman spectra of $Sn[CO_3]_2$ were calculated at 30 and 0 GPa and scaled by 5% and 10% to facilitate comparison with experiment. (b) Raman spectra of CO_2−V and $Ge[CO_3]_2$. Comparison of theoretical (blue line) versus experimental (black line) Raman spectra of $Ge[CO_3]_2$ at 49(4) GPa and 0 GPa. Theoretical frequencies of $Ge[CO_3]_2$ were calculated at 50 and 0 GPa and scaled by 4 and 9%, respectively, to facilitate the comparison with experiment. Theoretical (blue line) Raman spectra of CO_2−V were calculated at 30 and 50 GPa.

intense Raman band of $Sn[CO_3]_2$ is shifted at ∼393 cm^{-1}, and other prominent Raman bands are at ∼201, 265, 360, 729, 843, and 1119 cm^{-1} (Figure 6a). The DFPT calculations reproduce the experimental spectrum sufficiently well so that they can be employed to understand the corresponding vibrations. The required rescaling is very likely due to the use of a fully ordered model instead of a structure with partial site occupancies. On the basis of DFPT calculation, the most intense Raman bands of $Sn[CO_3]_2$ at 571 cm^{-1} (30 GPa) and 393 cm^{-1} (0 GPa) can be identified as the breathing mode of SnO_6 polyhedra. Symmetric stretching modes of isolated $[CO_3]$ groups have weak intensities and are located at 1178 cm^{-1} (30 GPa) and 1119 cm^{-1} (0 GPa). The other characteristic modes at 289 cm^{-1} (30 GPa) and 201 cm^{-1} (0 GPa) were assigned to the rotation mode of SnO_6 polyhedra. In the case of a quenched sample at ambient pressure, a narrow Raman band with a full width at half-maximum (fwhm) of 2 cm^{-1} was observed at ∼843 cm^{-1} in $Sn[CO_3]_2$ and can be attributed to the out-of-plane bending mode of $[CO_3]$ groups, whereas all other modes exhibit fwhm's in the range of 4−10 cm^{-1}. This small fwhm of the band may result from the absence of cations between the $[CO_3]$ groups, allowing the C atoms to move freely perpendicular to the $[CO_3]$ plane. Comparing the position of this Raman band with literature data, previous experimental studies have shown that this out-of-plane bending vibration occurs at 851−853 cm^{-1} in aragonite-type structures.[62] In contrast, it typically appears at higher frequencies, in the range of 860−881 cm^{-1} in calcite-type structures.[63]

In the case of $Ge[CO_3]_2$, characteristic Raman modes of $Ge[CO_3]_2$ can be observed unequivocally at ∼345, 510, 533, 635, 852, and 1228 cm^{-1}, in addition to the Raman modes of CO_2−V Figure 6b at 49(4) GPa. The most intense Raman band of $Ge[CO_3]_2$ is located at ∼635 cm^{-1} and shifted to ∼425 cm^{-1} at 0 GPa. Similar to $Sn[CO_3]_2$, this mode belongs to the breathing vibration of GeO_6 polyhedra. The rotation mode of GeO_6 polyhedra moved from 345 cm^{-1} (49 GPa) to 232 cm^{-1} (0 GPa). The position of symmetric stretching modes of isolated $[CO_3]$ groups changed from 1228 cm^{-1} (49 GPa) to 1137 cm^{-1} (0 GPa). Other modes of $Ge[CO_3]_2$ were observed at ∼331 and 386 cm^{-1}. The out-of-plane bending mode of $Ge[CO_3]_2$ was detected at 849 cm^{-1}, which is much closer to the corresponding values in aragonite-type structures than to those in $Sn[CO_3]_2$.[62] Unfortunately, some weak peaks overlapped with the Raman peaks of CO_2−V at high pressures.

Stability

We have shown that $Sn[CO_3]_2$ and $Ge[CO_3]_2$ can be formed by the reactions ($SnO_2 + 2CO_2 = Sn[CO_3]_2$ and $GeO_2 + 2CO_2 = Ge[CO_3]_2$) of GeO_2 and SnO_2 with CO_2. After the synthesis at high pressures and temperatures, we measured Raman spectroscopy during the decompression of the DAC. We did not observe any indication of a phase transition during pressure release. Furthermore, our Raman spectra clearly show that both carbonates can be recovered under ambient conditions.

Currently, we can only present a few constraints based on our experiments regarding the stability field of both carbonates. During brief heating at pressures ranging from 25 to 35 GPa, Ge carbonates were not readily formed. This might be the result of too low temperatures, or these conditions are just outside the stability field of carbonate formation. Therefore, the determination of the stability fields of $Sn[CO_3]_2$ and $Ge[CO_3]_2$ requires further theoretical and experimental studies.

CONCLUSIONS

Here, we present a detailed study of the synthesis, crystal structures, Raman spectra, and compression behavior of

https://doi.org/10.1021/acs.cgd.6c00352
Cryst. Growth Des. 2026, 26, 5436−5445

Downloaded from pubs.acs.org/cgdefu/article-pdf/26/14/5436/6531695 2/acs.cgd.6c00352.pdf by DEUTSCHES ELEKTRONEN-SYNCHROTRON user on 09 November 2026

$Sn[CO_3]_2$ and $Ge[CO_3]_2$. These compounds provide further examples of anhydrous, chemically simple carbonates incorporating tetravalent cations. The crystal structures of both compounds have been solved, and their characteristic Raman signatures have been established. The two carbonates are isostructural. Their structures are characterized by the presence of isolated $[CO_3]^{2-}$ groups and octahedrally coordinated Sn^{4+} and Ge^{4+} cations. The structures of both crystals are closely related to that of $Si[CO_3]_2$.[56] The main difference between $Si[CO_3]_2$ and the two phases obtained here lies in the out-of-plane tilting of the CO_3 groups in $Si[CO_3]_2$, which reduces the trigonal symmetry to monoclinic symmetry (Figure 2c).

The bulk moduli of $Sn[CO_3]_2$ and $Ge[CO_3]_2$ are relatively low, $K_0 \approx 44-48$ GPa, compared to typical calcite-type carbonates, which have bulk moduli in the range $\approx 60-130$ GPa.[60] The compressibility of $Sn[CO_3]_2$ or $Ge[CO_3]_2$ is very anisotropic, as their *c*-axes are more compressible than their *a*-axes.

The calcite structure type is built by a layered packing of $[CO_3]^{2-}$ groups and is well known to incorporate divalent cations spanning a wide range of ionic radii (0.45−1.0 Å).[7−9] Here we have demonstrated that related structures derived also from a layered packing of $[CO_3]^{2-}$ groups can accommodate tetravalent cations, such as Si, Ge, and Sn, also over a broad range of ionic radii (0.40−0.69 Å). Calcite-type structures are formed at low pressures, and it is well known that on pressure increase, numerous high-pressure phases with different packing of the $[CO_3]^{2-}$ groups are formed.[27] It is therefore to be expected that this also holds for the new structure type found here.

■ ASSOCIATED CONTENT

Supporting Information

The Supporting Information is available free of charge at https://pubs.acs.org/doi/10.1021/acs.cgd.6c00352.

> Experimental details of the single crystal synchrotron X-ray diffraction, crystallographic information, and the results of the single crystal structure solution and DFT-based calculations; pressure dependence of the relative unit-cell parameters; additional Raman spectra; and elastic stiffness constants and bulk moduli (PDF)

Accession Codes

Deposition Numbers 2531455−2531456 contain the supplementary crystallographic data for this paper. These data can be obtained free of charge via the joint Cambridge Crystallographic Data Centre (CCDC) and Fachinformationszentrum Karlsruhe Access Structures service.

■ AUTHOR INFORMATION

Corresponding Author

Lkhamsuren Bayarjargal − *Goethe University Frankfurt, Institute of Geosciences, 60438 Frankfurt, Germany;* orcid.org/0000-0002-5513-591X; Email: bayarjargal@kristall.uni-frankfurt.de

Authors

Dominik Spahr − *Goethe University Frankfurt, Institute of Geosciences, 60438 Frankfurt, Germany;* orcid.org/0000-0003-0489-5270

Elena Bykova − *Goethe University Frankfurt, Institute of Geosciences, 60438 Frankfurt, Germany;* orcid.org/0000-0001-8652-024X

Valentin Kovalev − *Goethe University Frankfurt, Institute of Geosciences, 60438 Frankfurt, Germany*

Victor Milman − *Dassault Systèmes BIOVIA, Cambridge CB4 0FJ, U.K.;* orcid.org/0000-0003-2258-1347

Nico Giordano − *Deutsches Elektronen-Synchrotron DESY, 22607 Hamburg, Germany;* orcid.org/0000-0001-9518-1251

Björn Winkler − *Goethe University Frankfurt, Institute of Geosciences, 60438 Frankfurt, Germany;* orcid.org/0000-0001-8029-478X

Complete contact information is available at: https://pubs.acs.org/10.1021/acs.cgd.6c00352

Notes

The authors declare no competing financial interest.

■ ACKNOWLEDGMENTS

We gratefully acknowledge funding from the DFG (projects BA4020 and WI1232) and the DFG-Research Unit FOR2125/CarboPaT. B.W. is grateful for support by the Dassault Systèmes Science Ambassador program. E.B. acknowledges the support of the DFG Emmy-Noether Program (project BY101/2-1) and the support of the Johanna-Quandt-Stiftung. We acknowledge DESY (Hamburg, Germany), a member of the Helmholtz Association HGF, for the provision of experimental facilities. Parts of this research were carried out at PETRA III, beamline P02.2.

■ REFERENCES

(1) Litasov, K.; Shatskiy, A.; Podborodnikov, I.; Arefiev, A.Phase diagrams of carbonate materials at high pressures, with implications for melting and carbon cycling in the deep Earth. In *Carbon in Earth's Interior* 2020; pp 137−165.

(2) Gao, J.; Wu, X.; Yuan, X.; Su, W. Fate of carbonates in the Earth's mantle (10−136 GPa). *Front. Earth Sci.* **2022**, *10*, No. 837775.

(3) Hazen, R. M.; Downs, R. T.; Jones, A. P.; Kah, L. Carbon mineralogy and crystal chemistry. *Rev. Mineral. Geochem.* **2013**, *75*, 7−46.

(4) Reeder, R. J., Ed. *Carbonates: Mineralogy and Chemistry*; Reviews in Mineralogy and Geochemistry; De Gruyter: Berlin, Boston, 1983.

(5) https://cnmnc.units.it, Updated list of IMA-approved minerals (May 2026). *International Mineralogical Association* 2024.

(6) Graf, D. L. Crystallographic tables for the rhombohedral carbonates. *Am. Mineral.* **1961**, *46*, 1283−1316.

(7) Liu, L.-G.; Lin, C.-C. A calcite → aragonite-type phase transition in $CdCO_3$. *Am. Mineral.* **1997**, *82*, 643−646.

(8) Shannon, R. D. Revised effective ionic radii and systematic studies of interatomic distances in halides and chalcogenides. *Acta Crystallogr., Sect. A* **1976**, *32*, 751−767.

(9) Spahr, D.; Bayarjargal, L.; Bykova, E.; Bykov, M.; Brüning, L.; Kovalev, V.; Milman, V.; Wright, J.; Winkler, B. 6-Fold-Coordinated Beryllium in Calcite-Type $Be[CO_3]$. *Inorg. Chem.* **2024**, *63*, 19513−19517.

(10) Bayarjargal, L.; Spahr, D.; Milman, V.; Marquardt, J.; Giordano, N.; Winkler, B. Anhydrous Aluminum Carbonates and Isostructural Compounds. *Inorg. Chem.* **2023**, *62*, 13910−13918.

(11) Bayarjargal, L.; Spahr, D.; Bykova, E.; Wang, Y.; Giordano, N.; Milman, V.; Winkler, B. High-Pressure Synthesis of an Iron Carbonate, $Fe_2[CO_3]_3$. *Inorg. Chem.* **2024**, *63*, 21637−21644.

(12) Wang, Y.; Bayarjargal, L.; Bykov, M.; Bykova, E.; Spahr, D.; Glazyrin, K.; Milman, V.; Winkler, B. Cr^{3+}-Containing Carbonates

Downloaded from pubs.acs.org/cgdefu/article-pdf/26/14/5436/6531695 2/acs.cgd.6c00352.pdf by DEUTSCHES ELEKTRONEN-SYNCHROTRON user on 09 November 2026

and Cr_2O_3-Pbcn at Extreme Conditions. *Inorg. Chem.* **2025**, *64*, 4996−5003.
(13) Spahr, D.; Bayarjargal, L.; Bruening, L.; Kovalev, V.; Bykova, E.; Bykov, M.; Milman, V.; Mezouar, M.; Winkler, B. Synthesis and Crystal Structure of Anhydrous Di-iodyl Carbonate $(IO_2)_2[CO_3]$, Hosting I^{5+}-Cations. *JACS Au* **2025**, *5*, 4675−4680.
(14) Bayarjargal, L.; Spahr, D.; Milman, V.; Giordano, N.; Giordano, N.; Milman, V.; Glazyrin, K.; Winkler, B. Synthesis and characterization of Ti^{4+} containing carbonates $Ti[CO_4]$ and $Ti_2O_3[CO_3]$. *Inorg. Chem.* **2025**, *64*, 21893.
(15) Spahr, D.; Bayarjargal, L.; Bykova, E.; Bykov, M.; Murphy, G. L.; Kegler, P.; Milman, V.; Giordano, N.; Winkler, B. High-pressure synthesis of $U_2[CO_3]_3$ and $U[CO_3]_2$ as potential host phases for uranium in the Earth's mantle. *Commun. Chem.* **2026**, *9*, No. 112, DOI: 10.1038/s42004-026-01911-0.
(16) McDonough, W. F.; Sun, S.-S. The composition of the Earth. *Chem. Geol.* **1995**, *120*, 223−253.
(17) Spahr, D.; Bayarjargal, L.; Kovalev, V.; Sharapova, N.; Brüning, L.; Jurzick, P. L.; Sebastian, S. S.; Bykov, M.; Milman, V.; Glazyrin, K.; Bykova, E.; Winkler, B. Silicon carbonate, $Si[CO_3]_2$, is a potential carbonhost in the deep Earth. *Sci. Adv.* **2026**, *12*, No. eaee5766, DOI: 10.1126/sciadv.aee5766.
(18) Tsuchida, Y.; Yagi, T. A new, post-stishovite highpressure polymorph of silica. *Nature* **1989**, *340*, 217−220.
(19) Murakami, M.; Hirose, K.; Ono, S.; Ohishi, Y. Stability of $CaCl_2$-type and α-PbO_2-type SiO_2 at high pressure and temperature determined by in-situ X-ray measurements. *Geophys. Res. Lett.* **2003**, *30*, No. 1207, DOI: 10.1029/2002GL016722.
(20) Kuwayama, Y.; Hirose, K.; Sata, N.; Ohishi, Y. The pyrite-type high-pressure form of silica. *Science* **2005**, *309*, 923−925.
(21) Haines, J.; Léger, J. X-ray diffraction study of the phase transitions and structural evolution of tin dioxide at high pressure: Relationships between structure types and implications for other rutile-type dioxides. *Phys. Rev. B* **1997**, *55*, 11144.
(22) Dutta, R.; Kiefer, B.; Greenberg, E.; Prakapenka, V. B.; Duffy, T. S. Ultrahigh-pressure behavior of AO_2 (A = Sn, Pb, Hf) compounds. *J. Phys. Chem. C* **2019**, *123*, 27735−27741.
(23) Sneed, D. T.; Smith, G. A.; Kearney, J. S.; Childs, C.; Park, C.; Lawler, K. V.; Salamat, A.; Smith, D. Stable and metastable structures of tin (IV) oxide at high pressure. *Philos. Trans. R. Soc., A* **2023**, *381*, No. 20220346, DOI: 10.1098/rsta.2022.0346.
(24) Ghosh, S.; Kumar, G.; Babu Pillai, S.; Dutta, R. Equation of state of the rutile and $CaCl_2$-type phases of GeO_2 to 70 GPa. *J. Appl. Phys.* **2025**, *138*, No. 235902, DOI: 10.1063/5.0302993.
(25) Boehler, R. New diamond cell for single−crystal X-ray diffraction. *Rev. Sci. Instrum.* **2006**, *77*, No. 115103.
(26) Mao, H. K.; Xu, J.; Bell, P. M. Calibration of the ruby pressure gauge to 800 kbar under quasi-hydrostatic conditions. *J. Geophys. Res.* **1986**, *91*, 4673−4676.
(27) Bayarjargal, L.; Fruhner, C.-J.; Schrodt, N.; Winkler, B. $CaCO_3$ phase diagram studied with Raman spectroscopy at pressures up to 50 GPa and high temperatures and DFT modeling. *Phys. Earth Planet. Inter.* **2018**, *281*, 31−45.
(28) Du, Z.; Amulele, G.; Benedetti, L. R.; Lee, K. K. M. Mapping temperatures and temperature gradients during flash heating in a diamond-anvil cell. *Rev. Sci. Instrum.* **2013**, *84*, No. 075111.
(29) Wojdyr, M. Fityk: a general-purpose peak fitting program. *J. Appl. Crystallogr.* **2010**, *43*, 1126−1128.
(30) Liermann, H.-P.; Konôpková, Z.; Morgenroth, W.; et al. The Extreme Conditions Beamline P02.2 and the Extreme Conditions Science Infrastructure at PETRAIII. *J. Synchrotron Radiat.* **2015**, *22*, 908−924.
(31) Prescher, C.; Prakapenka, V. B. DIOPTAS: a program for reduction of two-dimensional X-ray diffraction data and data exploration. *High Pressure Res.* **2015**, *35*, 223−230.
(32) Aslandukov, A.; Aslandukov, M.; Dubrovinskaia, N.; Dubrovinsky, L. Domain Auto Finder (DAFi) program: the analysis of single-crystal X-ray diffraction data from polycrystalline samples. *J. Appl. Crystallogr.* **2022**, *55*, 1383−1391, DOI: 10.1107/S1600576722008081.
(33) Sheldrick, G. M. SHELXT − Integrated space-group and crystal-structure determination. *Acta Crystallogr.* **2015**, *A71*, 3−8.
(34) Sheldrick, G. M. A short history of SHELX. *Acta Cryst. A* **2008**, *64*, 112−122.
(35) Sheldrick, G. M. Crystal structure refinement with SHELXL. *Cryst. Struct. Commun.* **2015**, *71*, 3−8.
(36) Dolomanov, O. V.; Bourhis, L. J.; Gildea, R. J.; Howard, J. A.; Puschmann, H. OLEX2: a complete structure solution, refinement and analysis program. *J. Appl. Crystallogr.* **2009**, *42*, 339−341.
(37) Hohenberg, P.; Kohn, W. Inhomogeneous Electron Gas. *Phys. Rev.* **1964**, *136*, B864−B871.
(38) Perdew, J. P.; Ruzsinszky, A.; Csonka, G. I.; Vydrov, O. A.; Scuseria, G. E.; Constantin, L. A.; Zhou, X.; Burke, K. Restoring the density-gradient expansion for exchange in solids and surfaces. *Phys. Rev. Lett.* **2008**, *100*, 136406.
(39) Clark, S. J.; Segall, M. D.; Pickard, C. J.; Hasnip, P. J.; Probert, M. I. J.; Refson, K.; Payne, M. C. First principles methods using CASTEP. *Z. Kristallogr.* **2005**, *220*, 567−570.
(40) *BIOVIA Materials Studio*; San Diego: CA, 2025.
(41) Lejaeghere, K.; Bihlmayer, G.; Björkman, T.; et al. Reproducibility in density functional theory calculations of solids. *Science* **2016**, *351*, No. aad3000.
(42) Monkhorst, H. J.; Pack, J. D. Special points for Brillouin-zone integrations. *Phys. Rev. B* **1976**, *13*, 5188−5192.
(43) Milman, V.; Warren, M. C. Elasticity of hexagonal BeO. *J. Phys.: Condens. Matter* **2001**, *13*, 241−251.
(44) Baroni, S.; de Gironcoli, S.; Dal Corso, A.; Giannozzi, P. Phonons and related crystal properties from density-functional perturbation theory. *Rev. Mod. Phys.* **2001**, *73*, 515−562.
(45) Refson, K.; Tulip, P. R.; Clark, S. J. Variational density-functional perturbation theory for dielectrics and lattice dynamics. *Phys. Rev. B* **2006**, *73*, No. 155114.
(46) Miwa, K. Prediction of Raman spectra with ultrasoft pseudopotentials. *Phys. Rev. B* **2011**, *84*, No. 094304.
(47) Aoki, K.; Yamawaki, H.; Sakashita, M.; Gotoh, Y.; Takemura, K. Crystal structure of the high-pressure phase of solid CO_2. *Science* **1994**, *263*, 356−358.
(48) Olijnyk, H.; Jephcoat, A. Vibrational studies on CO_2 up to 40 GPa by Raman spectroscopy at room temperature. *Phys. Rev. B* **1998**, *57*, 879.
(49) Scelta, D.; Dziubek, K. F.; Ende, M.; Miletich, R.; Mezouar, M.; Garbarino, G.; Bini, R. Extending the stability field of polymeric carbon dioxide phase V beyond the Earth's geotherm. *Phys. Rev. Lett.* **2021**, *126*, 065701.
(50) Datchi, F.; Giordano, V. M.; Munsch, P.; Saitta, A. M. Structure of carbon dioxide phase IV: Breakdown of the intermediate bonding state scenario. *Phys. Rev. Lett.* **2009**, *103*, No. 185701.
(51) Dziubek, K. F.; Ende, M.; Scelta, D.; Bini, R.; Mezouar, M.; Garbarino, G.; Miletich, R. Crystalline polymeric carbon dioxide stable at megabar pressures. *Nat. Commun.* **2018**, *9*, No. 3148.
(52) Lan, T.; Li, C. W.; Fultz, B. Phonon anharmonicity of rutile SnO_2 studied by Raman spectrometry and first principles calculations of the kinematics of phonon-phonon interactions. *Phys. Rev. B* **2012**, *86*, No. 134302.
(53) Micoulaut, M.; Cormier, L.; Henderson, G. The structure of amorphous, crystalline and liquid GeO_2. *J. Phys.: Condens. Matter* **2006**, *18*, R753−R784.
(54) Prakapenka, V.; Shen, G.; Dubrovinsky, L.; Rivers, M.; Sutton, S. High pressure induced phase transformation of SiO_2 and GeO_2: difference and similarity. *J. Phys. Chem. Solids* **2004**, *65*, 1537−1545.
(55) Momma, K.; Izumi, F. VESTA 3 for three-dimensional visualization of crystal, volumetric and morphology data. *Appl. Crystallogr.* **2011**, *44*, 1272−1276.
(56) Spahr, D.; Bayarjargal, L.; Kovalev, V.; Sharapova, N.; Bykova, E.; Winkler, B.; Bruening, L.; Jurzick, P.; Sebastian, S.; Bykov, M.; Milman, V.; Mezouar, M. Synthesis and crystal structure of anhydrous silicon sp^2-carbonate $Si[CO_3]_2$. *Sci. Adv.* **2026**, *12*, No. eaee5766.

Downloaded from pubs.acs.org/cgdefu/article-pdf/26/14/5436/6531695/2/acs.cgd.6c00352.pdf by DEUTSCHES ELEKTRONEN-SYNCHROTRON user on 09 November 2026

(57) Murnaghan, F. Finite Elastic Strain of Cubic Crystals. *Proc. Natl. Acad. Sci. U.S.A.* **1944**, *30*, 244−247.
(58) Birch, F. Finite Elastic Strain of Cubic Crystals. *Phys. Rev.* **1947**, *71*, 809.
(59) Angel, R. J.; Alvaro, M.; Gonzalez-Platas, J. EosFit7c and a Fortran module (library) for equation of state calculations. *Z. Kristallogr. - Cryst. Mater.* **2014**, *229*, 405−419.
(60) Zhang, J.; Reeder, R. J. Comparative compressibilities of calcite-structure carbonates: Deviations from empirical relations. *Am. Mineral.* **1999**, *84*, 861−870.
(61) Liang, W.; Yin, Y.; Li, Z.; Li, R.; Li, L.; He, Y.; Dong, H.; Li, Z.; Yan, S.; Zhai, S.; Li, H. Single crystal growth, crystalline structure investigation and high-pressure behavior of impurity-free siderite ($FeCO_3$). *Phys. Chem. Miner.* **2018**, *45*, 831−842.
(62) Bishop, J. L.; King, S.; Lane, M.; Brown, A.; Lafuente, B.; Hiroi, T.; Roberts, R.; Swayze, G.; Lin, J.-F.; Sánchez Román, M. Spectral properties of anhydrous carbonates and nitrates. *Earth Space Sci.* **2021**, *8*, No. e2021EA001844.
(63) Kim, Y.; Caumon, M.-C.; Barres, O.; Sall, A.; Cauzid, J. Identification and composition of carbonate minerals of the calcite structure by Raman and infrared spectroscopies using portable devices. *Spectrochim. Acta, Part A* **2021**, *261*, No. 119980.

Downloaded from pubs.acs.org/cgdefu/article-pdf/26/14/5436/6531695 2/acs.cgd.6c00352.pdf by DEUTSCHES ELEKTRONEN-SYNCHROTRON user on 09 November 2026

https://doi.org/10.1021/acs.cgd.6c00352
Cryst. Growth Des. 2026, 26, 5436−5445